International Conference on Mathematics, Computational Methods & Reactor Physics (M&C 2009)
Saratoga Springs, New York, May 3-7, 2009, on CD-ROM, American Nuclear Society, LaGrange Park, IL (2009)

VERIFICATION AND VALIDATION OF DETERMINISTIC RADIATION TRANSPORT NUMERICAL METHODS, CODES, AND NUCLEAR DATA FOR ESTIMATING RADIATION DOSE TO PATIENTS DURING CT SCAN

Joshua M. Hykes, Yousry Y. Azmy, and Sebastian Schunert
Department of Nuclear Engineering
North Carolina State University
Raleigh, NC 27695
jmhykes@ncsu.edu; yyazmy@ncsu.edu; snschune@ncsu.edu

Steven H. King
Milton S. Hershey Medical Center
Pennsylvania State University
Hershey, PA 17033
sking@psu.edu

Jesse J. Klingensmith
AREVA Federal Services
Lynchburg, VA 24501
jesse.klingensmith@areva.com

ABSTRACT

The goal of this work is to determine the viability of modeling an important x-ray procedure, the computed tomography (CT) scan of a pregnant woman and her conceptus using a deterministic radiation transport program. A prior experimental study provides the deposited dose as measured in an anthropomorphic phantom, with detectors positioned in the estimated uterine location. In this paper, we first verify the discrete ordinates code TORT3.2 and a suitably constructed multigroup cross section library against the Monte Carlo code MCNP5. Using MCNP, we demonstrate that accounting for the transport of secondary electrons is unnecessary in tissue-equivalent material. After demonstrating proper verification, we proceed to validate the MCNP and TORT simulations against data measured for the CTDI FDA phantom. In the model, the computed edge-to-center dose ratio is within experimental uncertainty, while the computed exposures are less than 35% from the measured values.

Key Words: CT scan, deterministic transport, medical physics, verification, validation

1. INTRODUCTION

Computed tomography (CT) imaging has been increasingly employed in medical diagnostic applications in the past three decades. While CT is a powerful imaging modality, it unfortunately imparts greater radiation dose as compared to traditional projection radiography. For instance, although only 12% of medical examinations performed in the US in the year 2006 were CT scans, they were responsible for 45% of the aggregate dose delivered to American patients [1]. Additionally, a typical abdominal CT scan deposits 30 to 50 mGy in the patient, 200-300 times

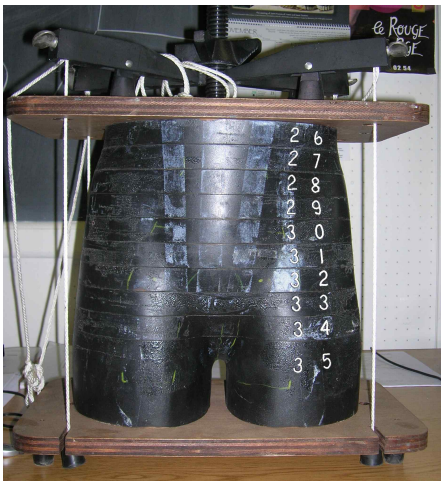

Figure 1: The Rando phantom anterior in its holding brace. The slice numbers are colored for better visibility.

the dose of a traditional chest x-ray [2]. Although this dose is usually deemed appropriate given the high quality of the resulting image data, estimating the dose is still an important task in judging the merits of a particular scan. Especially crucial is the determination of dose for a pregnant woman because subjecting the conceptus to elevated radiation levels can lead to mental retardation [3] and increased risk of childhood cancer [4]. To better quantify the conceptus dose, experimental tests were conducted at Hershey Medical Center (HMC) with an anthropomorphic Rando phantom [5] (see Fig. 1) in which the dose was measured using thermoluminescent dosimeters [6].

In cooperation with HMC's health physics staff who conducted this study, we seek to develop a solid foundation for the computational tools necessary to obtain accurate estimates of the radiation dose using state-of-the-art radiation transport numerical simulations. We accomplish this through a rigorous verification and validation procedure designed to test the performance of radiation transport computer codes and nuclear data in configurations representative of human anatomy subjected to radiological sources. Much attention has been paid to Monte Carlo methods for the solution of this problem. In contrast, little work has been attempted in applying deterministic methods. Deterministic transport methods generally have shorter execution time, provide the dose distribution over the entire irradiated region, and are well suited to model CT scan configurations, since the geometry is mapped into voxels. We use a state-of-the-art discrete ordinates code, TORT3.2, as the primary computational tool, while using MCNP5 to provide reference dose values for verification purposes.

We begin with a discussion of previous computational CT models. Next, the verification stage is presented, with tests for charged particle equilibrium and the multigroup approximation. Finally, we demonstrate the validity of the computational model and data for this application.

2. PREVIOUS COMPUTATIONAL MODELS

The radiation dose from CT scans is an important safety concern, prompting much research into both experimental and computational means to estimate the dose to patients. When one further considers similar work for other radiographic medical procedures, a large body of research exists on radiation dose from medical x-rays.

Monte Carlo Methods Monte Carlo methods are commonly employed in modeling CT scans. The method is able to capture the relevant physical phenomena, without the need to use assumptions or make abstractions required by deterministic methods. One major example of this is the continuous-energy modeling of particle histories as opposed to the multigroup approximation necessary in deterministic transport. In addition, secondary charged particles can be simulated in a natural way. Deterministic methods require altering the cross sections to account for the transport of charged particles in an efficient manner, and lack a simple means to track the movement of the charged particles after their creation. Unfortunately, even with biasing methods, Monte Carlo methods are still impractical for clinical applications. In 1997, when Larsen published his tutorial on radiation transport for oncology applications [7], it was generally accepted that Monte Carlo methods were roughly 1000 times too expensive. For the technology to be widely accepted, the simulation time must be around 10 minutes, a difficult goal for MC methods. For one-time calculations, this long run time is of little concern, but for production runs such a burden can be debilitating.

The review paper [8] summarizes the work in MC simulation of CT scans. The ability of MC codes to accurately estimate internal doses has been validated using the production codes MCNP [9] and EGS4 [10]. The MCNP paper [9] is especially relevant since this is the same program used in this work. For that study, the authors based their model on a General Electric Medical Systems scanner with both axial and spiral modes. The computational model was validated using the CTDI FDA head and body phantoms, acrylic glass cylinders 15 cm in length and 16 and 32 cm in diameter, respectively. The authors reported 8% agreement in the measured and computed doses at the center and 6% at the periphery over all tube potentials and slice thicknesses for the CTDI FDA phantom.

Deterministic Methods This paper focuses on the application of deterministic radiation transport methods to CT dose estimation. A description of representative deterministic methods is available in Lewis and Miller [11]. In contrast to Monte Carlo methods, full deterministic models are much less common in medical physics. Note that many deterministic algorithms are employed for dose calculations, but mostly these are grossly approximate methods such as the pencil beam approach. Although there is not much existing work, some research efforts have been made in preliminary application of deterministic methods to radiography and radiotherapy motivated by these methods' computational efficiency [12]. One paper describes an integral transport equation-based deterministic computer program for the computation of CT dose [13]. Because the program takes the geometrical input from CT data, the number of computational cells is large. On a 64-node high-performance cluster, the execution time was 4 minutes for the uncollided flux and 120 minutes for the scattered flux. Although the paper demonstrated the potential of

deterministic methods, in this case the required compute power is even greater than that necessary for a MC simulation.

Looking beyond CT, there are additional medical physics applications of deterministic codes. In one model of external beam therapy, the deterministic code TORT achieved good agreement with a Monte Carlo code named EGSnrc for parallelepiped-shaped cells (*voxels*) within the beam. Poor results were obtained for cells on the beam edge, where a sharp flux gradient existed [12]. The commercial finite-element code Attila has been benchmarked against MC methods for radiotherapy applications, both for a brachytherapy source and an external beam. For the brachytherapy problem, the difference in the calculated doses was less than 2% for the majority of the spatial extent, although some errors up to 5% were observed. The MC simulation took 990 minutes, while the Attila calculation lasted 20 minutes. For the external beam, the largest observed error was 2.2%. Much of the reported work has been in the area of Boron Neutron Capture Therapy (BNCT), an especially challenging computational undertaking because of the multiple modes of dose deposition involved. In work reported by Ingersoll *et al.*, a human leg undergoing BNCT was modeled in TORT with a disk source. The results from a MC calculation agreed to within 10 percent of the TORT answers. TORT ran three times faster than the MCNP model. The authors concluded that TORT, and other deterministic models in general, are well suited to solve problems on voxel-based anatomical models [14].

3. VERIFICATION OF DETERMINISTIC MODEL

Before modeling the anthropomorphic phantom, we build a very simple simulation to verify the capabilities of TORT. Since our ultimate goal is to simulate the Rando phantom, this model has the same tissue-equivalent material composition (see Table I). The density is 0.997 g/cc, the listed density of the phantom [5]. Instead of modeling the geometric irregularities at this preliminary stage, we approximate the phantom using a right circular cylinder with 13 cm radius, making the phantom dimensionally similar to the Rando slice of interest. To minimize axial variation of the flux near the middle of the cylinder height, the cylinder is 60 cm tall. Two small detector cylinders, of diameter 1 cm and height 2.54 cm and with the same material composition as the phantom, are located within the main cylinder, one along the cylinder axis and the other at the midpoint of a radius as illustrated by Fig. 2. We compute the group scalar fluxes and energy deposition at these two locations. Surrounding the cylinder is a thin cylindrical shell from which the x-rays are emitted isotropically. Since the peak tube potential in a CT scan is 120 or 140 kV, we choose an x-ray source with a maximum energy of 150 keV. As long as it is consistent between TORT and MCNP, the source spectrum is not particularly important at this stage, so we make the source monoenergetic, with energy 150 keV.

3.1. Secondary Electron Transport Treatment

One possible difficulty in using deterministic methods for medical physics applications is simulating secondary electron transport. We use a series of MCNP5 tests to determine the importance of the secondary electron transport. One can exploit the differences in the available MCNP tallies, as well as the photon-only versus photon-electron modes, to make this determination. Two distinct MCNP5 tallies are available to measure energy deposition. First, the F6 tally records energy lost during individual interactions of the sampled particle with the cell's

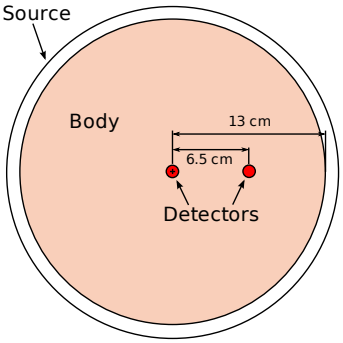

Figure 2: The simplified body cylinder MCNP model.

material content. The tally is based on the total track-length of the particles while they travel through the cell's volume [15]. The track length gives an estimate of the scalar flux, which relates directly to particle interaction rates and deposited energy. According to page 2-86 of the MCNP5 manual, all energy transferred to electrons is assumed to be deposited locally. Thus, the F6 tally is a measure of the kerma.

In contrast, the *F8 tally maintains a net sum of the energy of the particles entering and leaving a specified volume. An entering particle's energy is added to the total, while an exiting particle's energy is subtracted. This tally tracks the original particle as well as its progeny of secondary particles. Therefore, this tally does not assume secondary electron energy deposition to be local. This is useful because it enables two separate methods to test the validity of the hypothesis. First, using the photon-electron mode in which MCNP tracks the trajectories of both particle types, the *F8 and F6 tallies can be compared. If the kerma of F6 is approximately equal to the energy deposition of *F8, then charged particle equilibrium (CPE) for electrons exists. Second, the *F8 tally can be used to compare the dose computed via the photon-only to the dose computed via the photon-electron mode. In the photon-only mode, all energy transferred to electrons generated as secondary particles is assumed to be deposited locally, implying infinitesimally short electron trajectories from point of birth to point of total absorption.

Table I: Model material specifications [5].

Element	Weight Percent
Carbon	67.78
Oxygen	20.31
Hydrogen	9.18
Nitrogen	2.50
Antimony	0.22

F6 to *F8 Tally Comparison The MCNP5 manual states that the F6 and *F8 tallies should give the same total deposited energy provided CPE exists [15]. The present case was executed in photon-electron mode, and the F6 and *F8 tallies were compared for each of the center and radius detector volumes. The simulations were executed with 10^{10} particle histories. For the center detector, the relative difference between the F6 and *F8 tallies is 1.2%, and for the radius detector it is 0.8%. These errors are greater than the statistical uncertainty estimated by MCNP as 0.05% for the center detector and 0.18% for the radius detector. However, the relative difference of only a percent, while statistically significant, is practically negligible. Table II provides the tally data comparison for the photon-electron mode case. This close agreement is evidence that CPE exists and that secondary electron *transport* can indeed be neglected in this representative configuration.

Table II: The F6 and *F8 tally comparison confirms that CPE exists.

	F6		*F8		
	Dep. Energy (eV/g)	Relative Error	Dep. Energy (eV/g)	Relative Error	Relative Difference
Center	0.5785	0.0005	0.5855	0.0018	0.012
Radius	0.6487	0.0005	0.6539	0.0017	0.008

Photon-only to Photon-Electron Mode Comparison The second method of confirming that secondary electron transport is negligible in computing the deposited energy from a CT scan is utilizing the MCNP5 execution options of photon transport only and photon-electron transport. In the photon-only mode, energy transferred to electrons is assumed to be deposited locally. The *F8 tally is used to compare these two modes, as it tallies all particles entering and leaving the detector volume. Again, the simulations were executed with 10^{10} particle histories. The relative difference between the computed dose using these two modes for the center detector is 0.3%, while the MCNP statistical uncertainty for that detector is 0.18%. For the radius detector, the relative difference is 0.1%, and the statistical error is 0.17%. This statistical agreement again confirms the hypothesis that CPE holds in representative CT scan configurations. It is clear that the total energy deposited is practically the same for both modes. Avoiding the electron transport yields no significant difference in the computed total energy deposition. The results of these numerical experiments are summarized in Table III.

Internal Voids and Bones The CPE tests to this point have assumed that the phantom is homogeneous. While this is true of many phantoms, it is not valid for the Rando phantom and is especially egregious for a patient. Thus, we conducted similar tests using MCNP models which include two possible heterogeneities: internal voids and bones. Fig. 3 demonstrates how these components were added to the model. In both of these simulations, the difference between the dose with secondary electron transport and without secondary electron transport was either

statistically insignificant or significant but in the one percent range. Thus, we conclude that even in the presence of material heterogeneities, the transport of secondary electrons is not important.

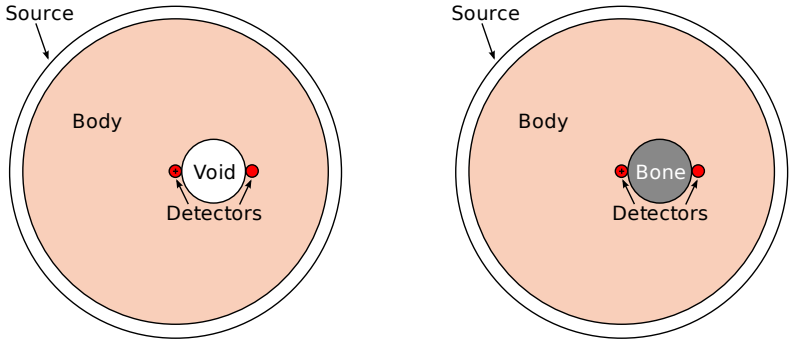

(a) Cylindrical phantom with void. (b) Cylindrical phantom with bone.

Figure 3: The simplified body cylinder MCNP model with an internal void and bone.

3.2. Multigroup Energy Verification using CTDI FDA Phantom

With the secondary electron transport hurdle cleared, we move on to a common challenge in deterministic transport—the multigroup energy approximation. To add more realism to the computational model, this simulation is based on the CTDI FDA body phantom, a right cylindrical homogeneous solid with five drilled holes for the placement of detectors. This is the phantom that was used during subsequent experimental measurements conducted at Hershey Medical Center. The CTDI FDA phantom is similar to the simple model used above, with a few exceptions. The phantom is made from polymethyl-methacrylate, also known as PMMA and acrylic glass, whose chemical formula is $C_5O_2H_8$. The cylinder is 32.0 cm in diameter for the body and 16.0 cm for the head phantom. The center hole is aligned along the cylinder axis, while the peripheral holes are at depth 1 cm from the surface, parallel to the axis. The density is 1.19 g/cc. The manufacturer's specifications state the height of the particular phantom used in the experimental measurements as 15 cm. A distribution of photon energies characteristic of a

Table III: The photon-only to photon-electron mode comparison using the *F8 tally also confirms the insignificance of accounting for secondary electron transport.

	Photon-only		Photon-Electron		
	Dep. Energy (eV/g)	Relative Error	Dep. Energy (eV/g)	Relative Error	Relative Difference
Center	0.5837	0.0018	0.5855	0.0018	0.003
Radius	0.6533	0.0017	0.6539	0.0017	0.001

tungsten x-ray tube was used. The details of how this distribution was obtained are left for the next section, where they fit more closely with the validation exercise. TORT was selected as the deterministic transport code that executes the model [16]. To build the geometry input for TORT, the companion program BOT3P is helpful [17]. Since TORT only handles Cartesian or cylindrical meshes in three-dimensional geometries, directly creating the input for TORT can be time consuming. BOT3P allows for the description of larger geometric bodies, which it then translates into a set of mesh cells based upon the given mesh spacing and writes them to a file in the format required by TORT for easy incorporation into its input file.

NJOY, the nuclear data processing code, was used to convert the point-wise continuous cross sections in the ENDF/B-VII photoatomic data libraries to multigroup sets appropriate for this application. The two main factors to consider when performing the multigroup collapsing are the energy group structure and the flux energy-dependence weighting factor. Many photon cross section sets use logarithmic divisions to encompass a wide range of photon energies. Thankfully, the photon energies of importance in the CT scan only range from about 1 keV to 150 keV. There are no photons with energies above the peak tube potential. With these factors in mind, the group structure is chosen with constant energy width. Ten groups from 10^{-4} eV to 200 keV are selected, with a width of 20 keV for each group. This is the first attempt at a group structure. This could, and probably should, be modified as more details about the prevailing energy spectrum emerge, either merging groups together to increase computational efficiency or splitting groups to gain better resolution. The other challenge when collapsing multigroup cross sections is to set the weight factors required for the cross section averaging over each group. Based on the Monte Carlo spectrum generated, a constant assumption seemed a better fit, over most of the relevant energy range, for this problem. Thus, the initial cross sections were generated with a constant weight. Later, as the model is refined, the data can be recollapsed using a more realistic photon spectrum. A third order Legendre expansion was employed for representing the anisotropy of the scattering cross sections.

Using the program CRSRD [18], a multi-group cross section set was prepared which MCNP can read from the ENDF/B-VII data used in TORT. This process is not simply a matter of reformatting numerical data. Since the simulation employed anisotropic multi-group data with Legendre expansion of the scattering cross section, the MCNP format requires that the moments be transformed to probability distributions. There exist a number of methods to perform this transformation which are implemented in CRSRD. Thus, using CRSRD was necessary to produce a multigroup cross section set consistent with that used in TORT to enhance the relevance of the ensuing comparison of the TORT versus MCNP5 computed doses.

With the nuclear data in hand, we execute the computational simulations, which fall into two broad categories. First, the deterministic TORT computations that constitute the main thrust of this project were run. Within this category, there is a simulation with a fine spatial mesh and high-order angular quadrature and another with a coarse spatial mesh and lower-order angular quadrature. The meshes as generated by BOT3P were non-uniform to better approximate the curved circumference of the cylinder by staircasing. The coarse mesh had cells of approximately 1 cm on a side, while the fine mesh had 0.2 cm cell sides. The low-order quadrature was the level-symmetric S_6 while the high-order one was level-symmetric S_{16}. The other category is Monte Carlo simulation with MCNP5. This type includes both continuous energy and multi-group cross section data.

The results of the Monte Carlo and deterministic simulations are given in Fig. 4 for the center detector. Plotted in this figure is the group flux computed by TORT on the coarse and fine models described earlier; the group flux computed by MCNP using the corresponding multigroup cross section library; the flux as computed by continuous-energy MCNP simulation then binned over the same multigroup bins, and also over a finer binning. The maximum relative difference (excluding the lowest and highest energy groups) between the coarse mesh deterministic solution and the multigroup Monte Carlo results is 10% at the center and edge detectors. Comparing the fine mesh deterministic fluxes with multigroup Monte Carlo, the maximum difference (again ignoring the negligible flux in the lowest energy group) is 7% at both locations. This good agreement for the flux spectra at both locations between the coarse and fine mesh TORT and multigroup MCNP results verifies the deterministic and stochastic multigroup solution schemes. As for the comparison with continuous-energy MCNP, although all of the higher energy group fluxes computed by TORT exhibit modest agreement with the computed multigroup Monte Carlo fluxes, the simulated flux in the 20-40 keV group has significant deviations, where the relative error exceeds 100% in the center detector location. Unfortunately, this group is important since it accounts for roughly 30% of the energy deposition. Thus, it is necessary to compute a multigroup cross section set with weights closer to the actual flux shape if better agreement is to be achieved.

We attempted collapsing the cross sections with three different weight factors: the x-ray tube spectrum, the x-ray tube spectrum without the characteristic peaks, and the spectrum computed by MCNP at the center of the phantom. The MCNP-computed spectrum gave the lowest overall error. The results for this set are illustrated in Fig. 5. The 20 to 40 keV group still has the highest error, but it is only about 15%, a marked improvement. Certainly these results show that adjusting the weighting factors can improve the accuracy of the results. However, the obvious choices for the weighting factor failed to produce multigroup fluxes with less than 15% error.

4. VALIDATION OF DETERMINISTIC MODEL

For the validation to proceed, the remaining large deficiencies in the model must be resolved. This is mainly an issue of improving the fidelity of the x-ray source distribution, in energy, angle, and position.

4.1. X-ray Beam Details

Modern CT machine designs call for rotation of the x-ray tube with a fan-shaped beam [19]. Fig. 6a shows the fan beam in a cross section view of the machine. Since the beam spreads, it intersects with the entire body, giving more projection data in the same amount of time. Collimators shape the beam to the desired geometry, and filters selectively reduce the beam intensity. The axial collimators are shown in Fig. 6b. An important detail in CT filters is the *bowtie* filter. The purpose of this filter is to reduce the intensity of the x-rays on the edges of the fan beam. Since the edge of the beam travels through shorter trajectories within the patient, a lower intensity can still produce the same detector response as compared to the center. This technique significantly reduces skin dose. A general estimate of the flux intensity from the fan beam center to the edge is available in [20]. The intensity is similar to one-half period of a sine wave, with the flux at the edges about 10% of the intensity at the center.

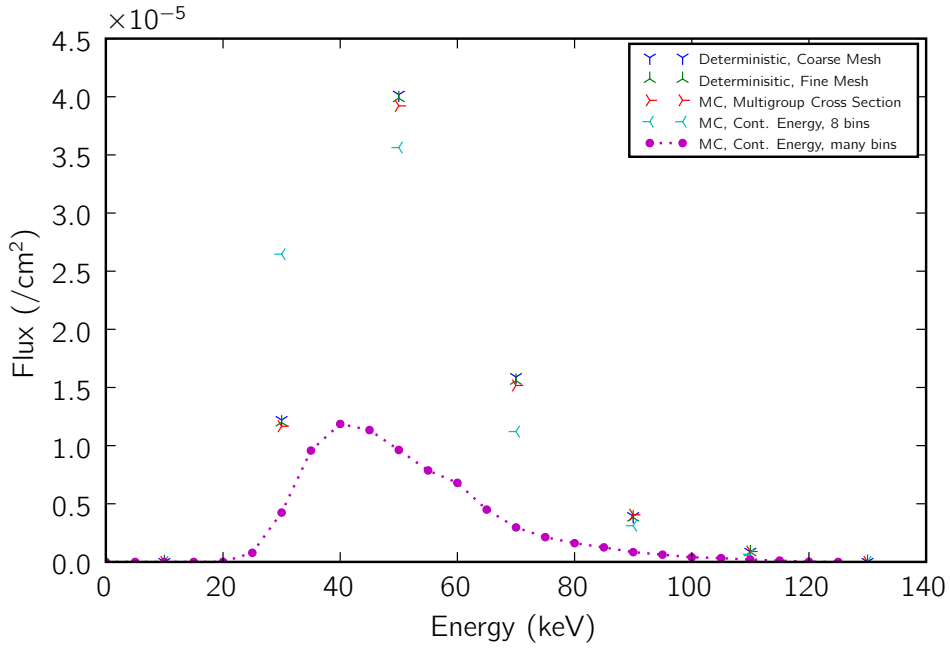

Figure 4: The computed flux at the center detector of the CTDI FDA phantom as computed with the constant-weighted multigroup cross section set.

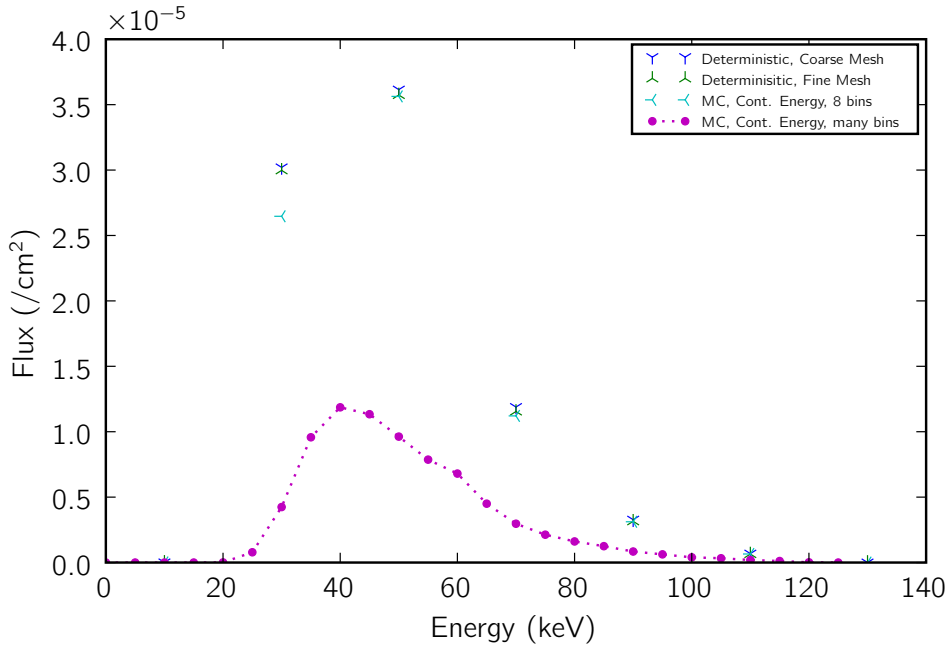

Figure 5: The flux at the center detector location of the CTDI FDA phantom as computed with the cross section set weighted by the flux spectrum computed by MCNP in the center of the phantom.

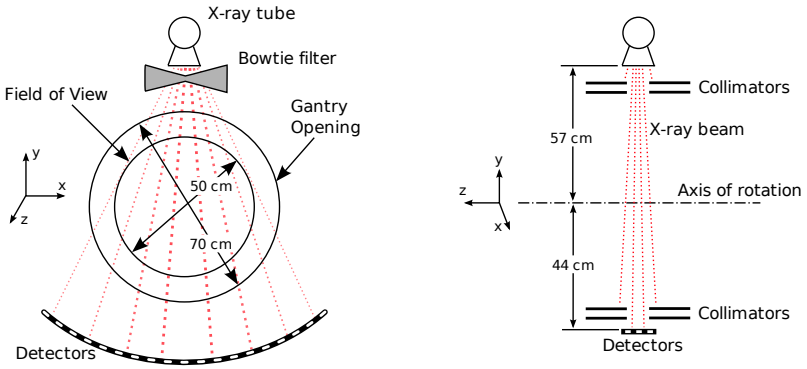

(a) CT cross section. (b) CT axial view.

Figure 6: The essential structure of the CT machine. The dimensions are typical of most CT machines [19].

The x-ray beam energy spectrum must also be included. The most direct and realistic approach would be the measurement of the x-ray spectrum using a radiation detector and multi-channel analyzer during one of the CT scans, positioning the detector at the center of the gantry without any phantom so that the measured spectrum would be similar to the spectrum incident on the phantom. Unfortunately, the radiologists at Hershey lacked the instruments necessary for this direct measurement, so another route must be forged. The literature is full of methods by which to obtain an x-ray beam spectrum, especially for x-ray tubes with tungsten anodes. In a frequently-cited paper on the subject [21], Boone and Seibert present a computer code written in C that generates the x-ray spectrum from a tungsten anode for 30 to 140 kV. This method uses measured x-ray spectra to interpolate for the desired beam. Using this program, the calculation of the beam spectra is simple. The main program inputs are the peak tube potential in kilovolts and the effective filtration thickness. The tube potential is a parameter set by the machine operator, so it is known for each measurement. In the experiments at Hershey, the peak tube potential was set to 120 kV. We estimated the filtration to be 5.0 mm Al by measuring the half-value layer of the beam.

In the verification stage, the simplest manner in which to deal with the x-ray beam intensity was to compute all results on a per-source-particle basis. However, to compare to the experiment, an absolute source strength is needed. Although one could estimate the intensity from the x-ray tube operating parameters (the scan time and current), a more direct route is to use the in-air measurement to scale the source. This requires an extra simulation of an in-air exposure, which is compared to the experimentally measured exposure to obtain an estimate for the absolute source intensity. This is the intensity after the filtration. This method is simple to apply, and is used in the following validation models. Also, it is consistent with other researchers' approach [9].

4.2. Implementing X-ray Beam Details in MCNP

Although preliminary simulations excluded the axial collimation and bowtie filter, we realized that these are important pieces of the model. MCNP offers much flexibility, so there are surely

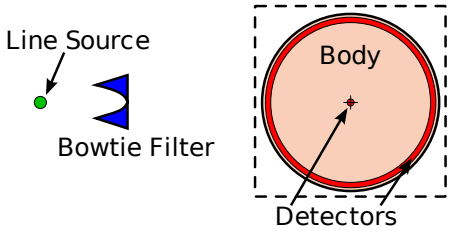

Figure 7: A cross section of the MCNP model with collimation and bowtie filter.

many ways to specify an appropriate source and corresponding phantom. The simplest model captures the relative motion of the source with respect to the phantom, where the x-ray source is fixed (rather than than the spiral trajectory it takes in the machine) and the body phantom is rotated. Since the CTDI FDA phantom is cylindrical and homogeneous, its rotation makes no difference except for the edge detector. To mimick the effect of the edge detector rotation, this small cylindrical detector is replaced with a cylindrical-shell detector, the volume of which is traced by the rotation of the original detector. A cross section of this is pictured in Fig. 7. To capture the translational motion of the source along the phantom axis, the x-ray beam is represented as a fixed line source parallel to the axis of the cylinder. The length of the line is equal to the CT scan length. Since the source is fixed, it is easy to insert a bowtie filter between the source and phantom. The axial collimation is accomplished by permitting source particles to begin only with angular cosines within the range defining the slice width. Note that if one deals with the ratio of the exposure (or energy deposition) in the edge to exposure (or energy deposition) in the center, then the source normalization is immaterial. This make the initial validation comparisons simpler.

We performed the MCNP simulation with the bowtie and collimation. For the experimental measurements at Hershey using the CTDI FDA phantom, the measured exposure was 1.96 R at the edge and 1.09 R at the center, giving a ratio of 1.8. Similarly, the optically-stimulated luminescent strips, which measure dose, have a ratio of 1.6. The MCNP-computed fluxes in the center and edge detector locations were folded with the appropriate response function to yield the integrated exposure over the 10-cm long detector. For the center, the exposure was 1.61×10^{-15} R and 2.69×10^{-15} R for the edge, both per source photon. The ratio of these two values is 1.68. In addition, the ratio of energy deposition in the edge to center is 1.73. These ratios are both in very good agreement with the experimentally measured values.

To scale the line source intensity, an in-air exposure simulation was run. The in-air exposure at the center was 8.60×10^{-15} R. Since the in-air measurement was 4.11 R, the source normalization factor is determined to be 4.78×10^{14}. Multiplying the source by this factor yields the results provided in Table IV. This model significantly underestimates the exposure at both the periphery and the center. However, errors of 34% for the edge and 28% for the center are not excessive when considering all the model simplifications and imprecise knowledge of several CT machine parameters.

Table IV: A comparison of the measured and simulated photon exposures with collimation and the bowtie filter.

	Exposure (R)	
Detector	MCNP	Measured
Edge	1.29	1.96
Center	0.78	1.08

4.3. Implementing X-ray Beam Details in TORT

After showing the importance of including collimation and the bowtie filter in MCNP, we turned to implementing these extra effects in the TORT model. The most obvious method to represent the collimation is to specify certain directions from the discrete ordinates quadrature set along which the source particles travel upon birth. Including the bowtie filtration is not as simple as in the MCNP model, so we overlooked this aspect temporarily. For the boundary source, the directions which lie closest to the scan plane have weights of one, and other directions have zero weights. This approach presents a number of difficulties. First, no directions in the quadrature set lie precisely in the scan plane. This is necessary to avoid division by zero in the discretized equation set. Unfortunately, most source particles should be traveling in the plane, so this is an obvious divergence from reality. The second problem is also a product of the discrete ordinates method. Since only a small fraction of the directions lie close to the scan plane, the majority of the directions are wasted. These issues contributed to noticeable ray effects in the model. This can be a problem in materials and energy groups that have a low within-group scattering ratio, which is true of the problem at hand. In addition, the detectors are small, so this makes the ray effects more damaging to solution accuracy because the rays are likely to miss the small detectors. To ameliorate the difficulties with ray effects, we used the program GRTUNCL3D to calculate the uncollided flux and first collision source with ray tracing. This is a semi-analytic method where the flux of photons that have avoided all interactions is computed at each spatial cell using the total cross sections and the exponential radiation attenuation law. With this additional step, the fluxes computed by TORT and MCNP without a bowtie filter exhibit better agreement, in the worst energy group a 19% difference, much improved from the difference of a factor of two or three caused by the ray effects.

However, this effort avoided the bowtie filter, and so it must be refined. Unfortunately, including the bowtie explicitly as in the MCNP model does not seem like a viable option. One alternate option which we are currently pursuing is the use of MCNP to model the x-ray source and entire filtration arrangement (including the bowtie) and use the resulting beam distribution to specify the incoming boundary flux for the TORT model. A possible boundary of this sort is shown in Fig. 7 as the dotted line. Since the phantom has negligible feedback on the source, the MCNP model should accurately capture the influence of the bowtie filter on the incoming flux to the phantom. Defining an appropriate boundary source would also be a general method, suitable for the CTDI FDA phantom as well as the Rando phantom.

5. CONCLUSIONS

We have demonstrated the feasibility of modeling the transport of CT x-rays through a phantom using deterministic computational models. First, we verified that the tracking of secondary electrons is unimportant for the computation of dose. In addition, the multigroup cross section set can be used with some confidence, as the greatest error in the computed fluxes was 15%. In the validation stage, the exposures computed from the simulation of the FDA phantom were roughly 30% from the measured value. The computed edge-to-center exposure ratio that scales-out the actual beam intensity was within experimental uncertainty, leading us to conjecture that the value we used in our model for the beam intensity is inconsistent with the actual value in the experimental setup. We must also note that the inputs, especially the source details, still contain a rather large degree of uncertainty. Knowing the exact beam rotation and position is nearly impossible, so we must use approximations and best estimates. In spite of these difficulties, a deterministic radiation transport code seems capable of modeling the dose during a CT scan with reasonable accuracy that we conjecture is possible to improve with better specification of the x-ray source distribution and intensity.

ACKNOWLEDGEMENTS

Part of this work was funded by the Centers for Disease Control grant NCSU#08-1020. The Department of Energy has also provided support through the Computational Science Graduate Fellowship of the first author.

REFERENCES

[1] F. A. Mettler, *National Council on Radiation Protection and Measurements*, Arlington, VA (2007).

[2] E. L. Nickoloff and P. O. Alderson, "Radiation Exposures to Patients from CT: Reality, Public Perception, and Policy," *American Journal of Roentgenology*, **177**, pp. 285–287 (2001).

[3] *Health effects of exposure to low levels of ionizing radiation, BEIR V*, National Research Council, Committee on the Biological Effects of Ionizing Radiation, National Academy Press, Washington, DC (1990).

[4] E. K. Osei and K. Faulkner, "Fetal doses from radiological examinations," *The British Journal of Radiology*, **72**, pp. 773–780 (1999).

[5] *Alderson Rando Phantom Systems for Radiotherapy*, Technical report, Alderson Research Laboratories.

[6] M. F. Dietrich, D. L. Miller, and S. King, "Determination of potential uterine (conceptus) doses from axial and helical CT scans," *Health Physics*, **88**, pp. S10–S13 (2005).

[7] E. W. Larsen, "The nature of transport calculations used in radiation oncology," *Transport Theory and Statistical Physics*, **26:7**, pp. 739–763 (1997).

[8] H. Zaidi and M.R. Ay. "Current status and new horizons in Monte Carlo simulation of X-ray CT scanners." *Medical and Biological Engineering and Computing*, **45(9)**, pp. 809817, 2007.

[9] G. Jarry, J.J. DeMarco, U. Beifuss, C.H. Cagnon, and M.F. McNitt-Gray. "A Monte Carlo-based method to estimate radiation dose from spiral CT: from phantom testing to patient-specific models." *Physics in Medicine and Biology*, **48(16)**, pp. 2645–2663, 2003.

[10] M. Caon, G. Bibbo, and J. Pattison. "An EGS4-ready tomographic computational model of a 14-year-old female torso for calculating organ doses from CT examinations." *Physics in Medicine and Biology*, **44**, pp. 2213–2226, 1999.

[11] E. E. Lewis and W. F. Miller, Jr. *Computational Methods of Neutron Transport.* American Nuclear Society, Inc., 1993.

[12] R. A. Lillie, D. E. Peplow, M. L. Williams, B. L. Kirk, M. P. Langert, T. L. Nichols, and Y. Y. Azmy. "Photon beam transport in a voxelized human phantom model: Discrete ordinates vs Monte Carlo." 14th Biennial Topical Meeting of the Radiation Protection and Shielding Division, pages 68–71, Carlsbad, NM, April 2006. American Nuclear Society.

[13] F. Inanc, "A CT image based deterministic approach to dosimetry and radiography simulations," *Physics in Medicine and Biology*, **47**, pp. 1–18 (2002).

[14] D. T. Ingersoll, C. O. Slater, E. L. Redmond, II, and R. G. Zamenhof. "Comparison of TORT and MCNP dose calculations for BNCT treatment planning." **75** of *Transactions of the American Nuclear Society*, pages 3637, Washington, DC, Decemeber 1996. American Nuclear Society.

[15] *MCNP—A General Monte Carlo N-Particle Transport Code, Version 5*, Los Alamos National Laboratory, April 2003.

[16] W. A. Rhoades and D. B. Simpson. The TORT Three-Dimensional Discrete Ordinates Neutron/Photon Transport Code. ORNL/TM-13221, 3rd edition, October 1997.

[17] R. Orsi. BOT3P Version 5.0: A Pre/Post-Processor System for Transport Analysis. ENEA Nuclear Data Center, April 2005. FIS-P9H6-008.

[18] J. C. Wagner, E. L. Redmond II, S. P. Palmtag, and J. S. Hendricks, "MCNP: Multigroup/Adjoint Capabilities," Los Alamos National Laboratory, LA-12704 (1994).

[19] Willi A. Kalender. *Computed Tomography*. Wiley, 2000.

[20] T. Toth, Z. Ge, and M.P. Daly. "The influence of patient centering on CT dose and image noise." *Medical Physics*, **34**, p. 3093, 2007.

[21] John M. Boone and J. Anthony Seibert. "An accurate method for computer-generating tungsten anode x-ray spectra from 30 to 140 kV." *Medical Physics*, **24(11)**, pp. 1661–1670, 1997.